Zweitveröffentlichung/
Secondary Publication

Staats- und
Universitätsbibliothek
Bremen

https://media.suub.uni-bremen.de

Mojtaba Mirdrikvand, Mehrdad Sadeghi, M. Nurul Karim, Jorg Thöming, Wolfgang Dreher

# Pore-scale analysis of axial and radial dispersion coefficients of gas flow in macroporous foam monoliths using NMR-based displacement measurements

| | | |
|---|---|---|
| Journal Article | as: | peer-reviewed accepted version (Postprint) |
| DOI of this document*(secondary publication): | | https://doi.org/10.26092/elib/2513 |
| Publication date of this document: | | 15/11/2023 |

* for better findability or for reliable citation

Recommended Citation (primary publication/Version of Record) incl. DOI:

Mojtaba Mirdrikvand, Mehrdad Sadeghi, M. Nurul Karim, Jorg Thöming, Wolfgang Dreher,
Pore-scale analysis of axial and radial dispersion coefficients of gas flow in macroporous foam monoliths using NMR-based displacement measurements,
Chemical Engineering Journal, Volume 388, 2020, 124234, ISSN 1385-8947,
https://doi.org/10.1016/j.cej.2020.124234

Please note that the version of this document may differ from the final published version (Version of Record/primary publication) in terms of copy-editing, pagination, publication date and DOI. Please cite the version that you actually used. Before citing, you are also advised to check the publisher's website for any subsequent corrections or retractions (see also https://retractionwatch.com/).

This document is made available under a Creative Commons licence.

The license information is available online: https://creativecommons.org/licenses/by-nc-nd/4.0/

Take down policy

If you believe that this document or any material on this site infringes copyright, please contact publizieren@suub.uni-bremen.de with full details and we will remove access to the material.

# Pore-scale analysis of axial and radial dispersion coefficients of gas flow in macroporous foam monoliths using NMR-based displacement measurements

Mojtaba Mirdrikvand[a,*], Mehrdad Sadeghi[b], M. Nurul Karim[a], Jorg Thöming[b], Wolfgang Dreher[a]

[a] University of Bremen, Department of Chemistry, In-vivo-MR Group, Leobener Str. 7, 28359 Bremen, Germany
[b] University of Bremen, Chemical Process Engineering, Leobener Str. 6, 28359 Bremen, Germany

## HIGHLIGHTS

- An NMR based pore-scale analysis of gas dispersion along open cell foams was suggested.
- Axial and radial dispersion coefficients were determined in spatially resolved measurements.
- The effect of open porosity, window size, and flow rate on gas dispersion was shown.
- The transition from diffusional to mechanically driven dispersion was determined.

## ARTICLE INFO

*Keywords:*
Dispersion coefficient
Axial and radial dispersion
NMR
Foam catalyst support
Gas

## ABSTRACT

A micro-scale analysis of mass transport in ceramic foams that are used as catalyst supports in gas phase reactions is of high interest. Although the effects of flow rate and foam parameters on the radial and axial dispersion are known for liquid flows, no pore-scale experimental analysis has been yet reported to correlate the mechanical and diffusional dispersion of gas flows to the geometry of open-cell foams. Here, a spatially resolved Pulsed Field Gradient NMR method is applied to determine dispersion coefficients of thermally polarized gas along axial and transversal directions of open-cell foams. The comparative study of three commercial foam samples with different morphologies shows the effect of open porosity, window size, and flow rate on gas dispersion. Additionally, the influence of mechanical and diffusional dispersion at each flow rate is investigated for individual samples. By observing the transition from diffusional dispersion to mechanically driven dispersion of gas, it is found that diffusional dispersion plays an important role, even at higher flow rates after a transition from Darcy to Darcy-Forchheimer regime occurs. The measured values for dispersion coefficients of methane can be directly used in pseudo-heterogeneous models for the methanation reaction.

## 1. Introduction

Open-cell foams have been increasingly considered in process engineering applications during the past 20 years [1–7]. The foams are being used as catalyst carriers in heterogeneously catalyzed gas phase reactions because of their low pressure drop, high specific surface area, and most importantly excellent mass and heat transport properties which enhance the local rate of the heterogeneous reactions [1,4,7]. The investigation of gas mass transport in opaque foams can directly support simulations using pseudo-heterogeneous models to predict gas phase reactions such as methanation of CO or $CO_2$. Among mass transport properties, dispersion coefficients in both radial and axial directions are of high interest to be used in the numerical simulations [8]. At macroscopic level, axial and radial dispersions of gas flow contribute to mass transport based on two-dimensional convection–diffusion equation (Eq. (1)) in cylindrical coordinates (r,φ,z), where $D_{\parallel}$ and $D_{\perp}$ are the axial and radial dispersion coefficient, respectively

$$\frac{\partial C}{\partial t} = D_{\parallel}\frac{\partial^2 C}{\partial z^2} - \bar{u}\frac{\partial C}{\partial z} + D_{\perp}\left(\frac{\partial^2 C}{\partial r^2} + \frac{1}{r}\frac{\partial C}{\partial r}\right) \tag{1}$$

The equation remains valid as long as mass transport occurs in path lengths greater than the characteristic pore size. In Eq. (1), $C$ stands for concentration, and $\bar{u}$ for average velocity [9–11]. Thus, the dispersion of gas in foams in both radial and axial direction is characterized by the dispersion coefficient ($D_{disp}$) and can be associated with contributions of diffusional and mechanical dispersion [12]. If an analytical method allows to measure dispersion coefficients in the validity range of Eq.

* Corresponding author.
*E-mail address:* mirdrikvand@uni-bremen.de (M. Mirdrikvand).

https://doi.org/10.1016/j.cej.2020.124234
Received 2 October 2019; Received in revised form 24 January 2020; Accepted 25 January 2020
Available online 27 January 2020
1385-8947/ © 2020 Elsevier B.V. All rights reserved.

(1), the results can be used in numerical solutions based on Eq. (1).

Although the effect of the foam's geometry on the mass transport properties has already been recognized [13,14], most often radial and axial dispersion coefficients have been predicted using merely the analogy between heat and mass transfer or conventional pulse tracer measurement methods. This is due to the great difficulties in precise measurements of gas dispersion to give a pore-scale analysis of gas spreading in foams. Nevertheless, several studies aimed to overcome these problems and described some geometry-dispersion related aspects using conventional tracer experiments, optical measurements such as particle image velocimetry (PIV), point-wise injection of a tracer, or spectroscopic methods like laser-induced fluorescence (LIF) [4,5,15–18]. For instance, the point-wise injection method was implemented to measure radial dispersion coefficients using various tracers [15,16]. Benz et al. injected methane as tracer to measure radial dispersion coefficients for 10, 20, 30, and 50 ppi foams [15]. Smoke, as another tracer, was used in short ceramic foams with different pore sizes measured at higher flow rates. Conventional tracer experiments were also used to measure the axial dispersion coefficients [4,18,19]. In these studies, axial dispersion was measured based on the tracer residence time and its distribution curves. Häfeli et al. used wire-mesh sensors as well as laser induced fluorescence in porous media, but no distinction in flow behavior was found to relate it to foams' geometrical properties [18,20,21]. PIV [1] and LIF [21] have also been applied to obtain radial dispersion coefficients of water flow in glass made foams with a certain scale-up factor. Although the mentioned studies reported verified values for low Peclet numbers *Pe*, lower accuracy and scarce experimental data yielded for higher flow rates a correlation between the velocity, and the characteristic pore diameter with ± 40% accuracy. In addition, no clear effect of window size, velocity and pore size on gas/liquid flow has been investigated in previous studies, as the majority of the methods focused on downstream and upstream flow and not on flow through the foams. Recently, a promising work has shown the use of magnetic resonance velocimetry (MRV) for water flow in a 40 ppi open-cell foam [22]. The 3D velocity map was used to investigate radial mixing. The effect of geometry on dispersion mechanisms was described to better understand the mechanisms of mass transport in foams for a single *Re* number. Streamline displacement was extracted to compute mechanical dispersion coefficients after post-processing of the full field MRV results. An exhaustive dispersion analysis for gas flow has still to be done to investigate a possible correlation between gas flow and the foam topology, both in transversal and in axial direction. Furthermore, velocity measurements allow to correlate the effect of *Re* numbers in Darcy and Darcy-Forchheimer regime on the dispersion to the foam morphology with a higher certainty compared to the traditional measurement methods.

Nuclear Magnetic Resonance (NMR) offers a variety of approaches in order to measure diffusion, flow, and dispersion of gases in porous media. An advantage of the NMR displacement measurements is their use of a Lagrangian coordinate system [23] by encoding the position of gas molecules prior to and after a certain displacement time, respectively. Labeling and de-labeling the gas molecules allow correlating fluid hydrodynamics to window size, pore diameter, and the open porosity of foams for a very short contact time between gas and solid. While often specific dispersion models are used in the field of chemical engineering [24,25], NMR directly reveals the information on path length of gas flow through the porous sample. In contrast to most measurement approaches, NMR keeps the measured system intact without tracers and no specially designed foam sample is needed in contrast to LIF.

Pulsed field gradient (PFG) sequences have already been used to map flow displacement, diffusion, and dispersion in porous media [26–28]. Since Seymour and Callaghan presented general approaches for flow dispersion measurement [29], several studies have been conducted to determine flow in porous media such as rocks or glass beads [12,30]. This approach has also been applied by other authors for water flow for Stokes regime [9]. Recently, Ferrari et al. have reported a dispersion analysis of water flow in packed bed at low flow rates [26]. Our study is mainly inspired by the work of Seymour and Callaghan [29], in which the dispersion of liquids was investigated in the axial and radial directions. However, this approach is applied to thermally polarized gas and a spatially resolved analysis is performed to observe the dispersion of gas in foams. Since the NMR displacement measurements label $^1$H protons of methane, no tracer is required in contrast to measurement techniques commonly used in the field of chemical engineering; thus, avoiding a disturbance in flow and making the measurement non-invasive. Accordingly, our recently optimized NMR sequence [31] was used in the current study to investigate mass transport of gas through monolithic foam supports with high accuracy. Here we report on the application of that method for gaining new insights into the combined effects of diffusion and flow (with different flow rates) on the displacement of molecules. In addition, we quantify the influence of window size, porosity, and intrinsic velocity of the gas on mass transport. In this study, the flow regime covers low and high *Pe* numbers for foams with different pore densities (10, 20, and 40 ppi) in order to analyze a broad range of gas flow similar to flow rates applied in the methanation reaction. In contrast to traditional measurements for foams (analysis at inlet and outlet), we determine pore-scale dispersion coefficients within the structures using a spatially resolved approach, which allows cross-validation of numerical simulations with the NMR results.

## 2. Theory and method

The resolution of PFG NMR displacement measurements (in micrometer range) exceeds the conventional spatial resolution that can be achieved in Magnetic Resonance Imaging (MRI). The PFG NMR with the capability of measuring displacements in a volume-of-interest (VOI) can be employed to conduct measurements in a certain part of a catalysts support in the reactor. This is contrary to common applications of PFG methods used for a global analysis of whole samples. Thus, the localized PFG NMR method is a powerful toolkit for measuring dispersion coefficients of gas in a certain VOI of open-cell foams [31] by tracking hydrogen ($^1$H) containing materials flowing through the porous medium. For thermally polarized gases, a considerably lower Signal-to-Noise Ratio (SNR) is expected as compared to liquids. This is mainly due to lower spin density and shorter transversal relaxation times $T_2$ in gases. Therefore, optimized PFG sequences are essential to minimize SNR losses to provide precise information on diffusion and flow in foams in μm range.

In this study a volume selective stimulated echo (STE) pulse sequence [32] was employed to measure displacement of gas in a desired volume element (Voxel) with arbitrary orientation. Fig. 1 displays the applied PFG-STE sequence. Asymmetric RF pulses were used to reduce the minimum echo time *TE* and consequently signal losses by $T_2$ relaxation [33]. Diffusion sensitizing gradients (columns with horizontal dashed lines in Fig. 1) in axial and radial direction are used between the first and the second 90° RF pulse as well as between the third RF pulse and the beginning of data acquisition. Rephasing or dephasing gradients were applied immediately after or prior to the slice selection gradients (cf. Fig. 1) to reduce diffusion weighting effects during slice selection. In addition, spoiler gradients were applied during the mixing time ($T_m$) and a two-step phase cycle was used for the first 90° pulse to suppress unwanted signal contributions. A detailed description of the optimized pulse sequence was given in a previous study on diffusiometry of methane gas in foams [31]. The basic principles of measuring translational displacement probabilities by NMR are described in previous studies [34–36]. For most measurements, a VOI of $12 \times 12 \times 12$ mm$^3$ was chosen to measure gas dispersion in a representative volume of the sample, including the sample center, where the flow mixes in the interconnected network of the foam's pores (cf. Fig. 2). Additionally, another VOI size of $16 \times 16 \times 16$ mm$^3$ was used

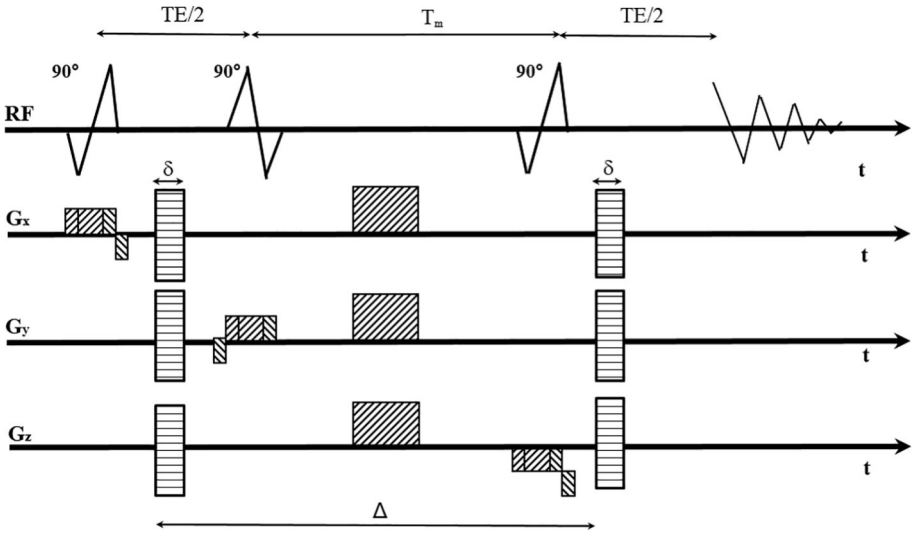


**Fig. 1.** Scheme of the applied PFG-STE sequence used for displacement measurements (not to scale). Voxel selection is performed by the three 90° pulses with orthogonal slice orientation. A two-step phase cycle and spoiler gradients within the mixing time $T_m$. are used to eliminate signals other than the stimulated echo.

to evaluate to what extent the voxel size affects the estimated radial and axial dispersion coefficients.

In case of unrestricted Gaussian diffusion, the diffusion coefficient or, more generally, the dispersion coefficient can be obtained from at least two measurements performed with different diffusion weighting described by the so-called *b*-value $b = \gamma^2 \cdot \delta^2 \cdot G_d^2 \left(\Delta - \frac{\delta}{3}\right)$, where $G_d$ is the amplitude of the two identical diffusion weighting gradients, $\delta$ is the duration of the diffusion sensitizing gradients, and $\Delta - \delta/3$ is the observation time. However, in this study the observation time can be approximated by $\Delta$ because $\frac{\delta}{3} \ll \Delta$ (cf. Section 3.2). The amplitude of the measured *STE* signal is given as a function of the dispersion coefficient $D$ by

$$S = S_0 \cdot e^{\frac{-TE}{T_2}} \cdot e^{\frac{-T_m}{T_1}} \cdot e^{-b \cdot D} \tag{2}$$

$S_0$ is the signal amplitude if relaxation losses and diffusion weighting are negligible. Relaxation losses during the echo time $TE$ are determined by the transverse relaxation time $T_2$, while during the mixing time $T_m$ the relaxation related signal decay depends on the longitudinal relaxation time $T_1$ (cf., Fig. 1).

By incrementing the $q$-value defined in Eq. (3), the echo signal may be written as a function of $q$ and the displacement probability $P$ [23,34,36] for the time interval $\Delta$.

$$q = \gamma \cdot \delta \cdot G_d \tag{3}$$

$$S(q) = \int \rho(r_0) \int P(r_0|r, \Delta) e^{iq(r-r_0)} dr dr_0 \tag{4}$$

Note that in all measurements $\delta \ll \Delta$ should be satisfied.

*Displacement function:* The displacement probability or, in other words, the gas propagator can be derived by Fourier transformation of the STE signal as function of $q$. Thus, the probability that spins have been displaced by the path length $(r - r_0)$ during the observation time $\Delta$ can be calculated. Some characteristic values can be used for the description of the gas propagators. For instance, the full width at half maximum (FWHM) $\Delta\nu_{1/2}$ is a characteristic that describes how wide the displacement is. The maximum displacement length ($\Delta L_{\max}$) can be calculated from the tails of the displacement probability, where the function approaches the x-axis. $\Delta L_{\max}$ indicates the maximal displacement of the gas ensemble within the given observation time for NMR measurement. This length can be compared to the window diameter of the foams samples at different flow rates.

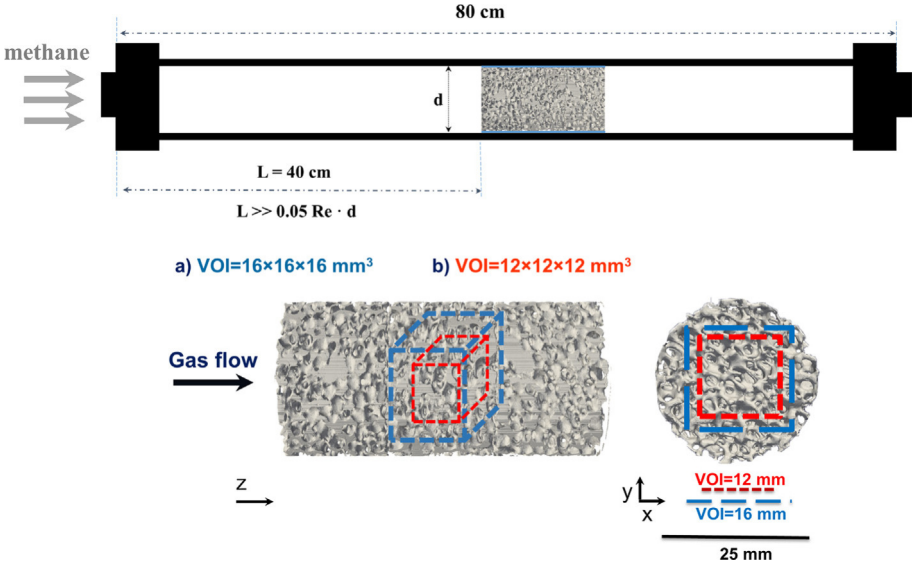


**Fig. 2.** Experimental setup and volumes-of-interest used for the PFG-STE measurements. a) VOI = 16 × 16 × 16 mm$^3$ and b) VOI = 12 × 12 × 12 mm$^3$.

*Dispersion coefficient:* In case of a Gaussian distribution, the dispersion coefficient $D$ can be calculated in two ways. Using the probability density for 1-dimensional Gaussian diffusion [37] the dispersion coefficient can be estimated by using its dependence on $\Delta\nu_{1/2}$:

$$D = (\Delta\nu_{1/2})^2/(16\log(2)(\Delta - \delta/3)) \quad (5)$$

or $D$ can be calculated by fitting the measured data to Eq. (2). If a log-linear fit of the initial time-domain signal or the peak area in the frequency domain versus $b$-values is used, data measured at large $b$-values should be excluded because deviations from the expected log-linear fit will occur at low SNR. In case of expected non-Gaussian probability distributions, the restriction to low $q$-values ("low $q$-value limit") is of particular importance because this range of $q$-values allows to estimate dispersion coefficients using only the data for $b{\cdot}D \ll 1$ as proposed by Seymour and Callaghan [23]. Alternatively, as mentioned before, the FWHM value of the probability distribution can be used to estimate $D$.

## 3. Materials and methods

### 3.1. Ceramic foams

$Al_2O_3$ foams (length: 23 mm, diameter: 25 mm, 10, 20, and 40 pores per inch (ppi); Hofmann CERAMIC GmbH, Breitscheid, Germany) were inserted into a cylindrical glass model reactor (length: 80 cm, inner diameter: 26 mm). Methane was supplied as probing gas through a mass flow controller (Bronkhorst Deutschland Nord GmbH, Kamen, Germany). The pressure was measured at the inlet and outlet of the experimental setup. In all measurements, the operational pressure and the temperature were 1.3 bar and 16–17 °C, respectively. The geometrical characteristics of the samples were obtained by µ-CT imaging (see Table 1, Fig. 3). The size of window diameter, pore density, strut diameter, and open porosity of the samples are given in Table 1. The samples were inserted tightly into the model reactor to prevent unwanted bypass flow through the free space between the samples and the reactor wall. The hydrodynamic entry length was long enough to ensure that the flow is fully developed when it enters the structure.

#### 3.1.1. Ceramic foam morphology

Different methods such as gravimetric analysis, tetrakaidecahedral unit cell model, and µ-CT volume imaging technique were utilized to characterize the morphological properties of the samples. The mass and volume of samples were measured by standard lab-scale and caliper. The open porosity, specific surface area, window, and pore distribution of samples were determined via image processing of a set of 2D µ-CT images. In this method, 3D representative elementary volumes of the sponges were reconstructed and then analyzed. The pore diameter was defined as mean diameter of spheres of equivalent volume. Finally, the strut diameter and the specific surface area of the foams were calculated from µ-CT data using the proposed unit cell model by Inayat et al. [38].

### 3.2. Flow characteristics

Various flow rates ranging from 0.10 to 2.25 L·min$^{-1}$ (inlet superficial velocity: 3.39–76.39 mm·s$^{-1}$) were applied to investigate gas dispersion in axial and radial direction. The flow regime can be described with dimensionless numbers. The calculation of the Reynolds number *Re and* $Re_p$, is based on Eq. (6) using $u$ for the intrinsic velocity of gas bulk, $\nu$ for the dynamic viscosity, and either the diameter of the reactor $d$ or the mean pore diameter $d_p$ of each foam. The Peclet number $Pe$ is defined by Eq. (7) with $D_{eff}$ being the effective diffusion constant of methane in the absence of flow.

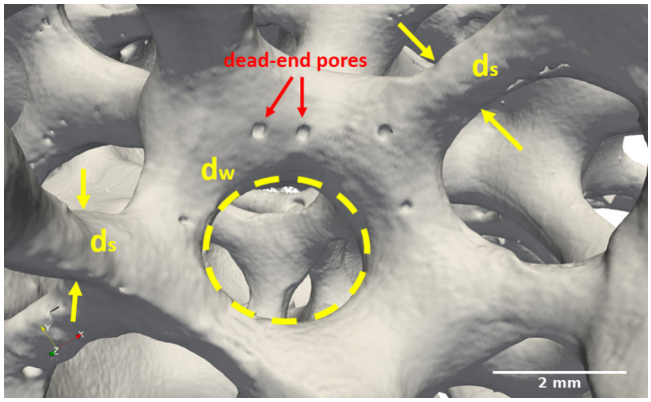


**Fig. 3.** Characteristics of foam in a typical µ-CT image: window diameter ($d_w$), strut diameter ($d_s$), and dead-end pores.

$$Re_{(p)} = \frac{u_{bulk} \cdot d_{(p)}}{\nu} \quad (6)$$

$$Pe = \frac{u_{bulk} \cdot d}{D_{eff}} \quad (7)$$

The calculated pore Reynolds number ($Re_p$) values are in a range of 0.48–24.51. The applied flow rates correspond to Reynold numbers ($Re$) based on the reactor diameter ranging from 5 to 114 and $Pe$ numbers of 3.85–86 for the bulk flow. Therefore, the bulk flow remains in the Darcy and Darcy-Forchheimer regime, wherein the flow is dominated by inertial forces [39–41].

### 3.3. NMR displacement measurements

A 7 Tesla preclinical NMR imaging system (Biospec 70/20, Bruker Biospin GmbH, Ettlingen, Germany) equipped with a gradient system BGA12S2 (maximum gradient strength of 441 mT/m in each direction, rise time 130 µs) was used for all measurements. For RF excitation and signal detection a quadrature birdcage RF coil (inner diameter of 72 mm) was used. Paravision 5.1 was used as the interface for implementing the pulse sequence and performing the PFG NMR measurements.

Prior to each measurement the samples were imaged using a 3D gradient-echo MRI sequence in order to adjust the VOI. The parameters were as follows: Repetition time $TR$: 25 ms, echo time $TE$: 0.5 ms, flip angle: 45°, two averages, Field-of-View (FOV): 64 × 64 × 96 mm$^3$, matrix size: 192 × 192 × 16, total measurement time: 2 min 33 s.

The volume selective PFG-STE sequence used asymmetric 90° RF pulses of 500 µs duration, voxel size: 12 × 12 × 12 or 16 × 16 × 16 mm$^3$, 64 equidistant $q$-space values, displacement range ± 5 mm, 1024 complex data points sampled with 25 kHz. For $^1$H measurements of methane performed at 300 MHz, ambient temperature, and atmospheric pressure, a $T_1$ value of 20–25 ms is expected [42]. Thus, saturation effects were avoided by using a repetition time of

**Table 1**
Characteristics of foams (a: µ-CT, b: tetrakaidecahedral unit cell model).

| Sample/Pore density (ppi) | Open porosity[a] ($\varepsilon$) | Pore diameter[a] ($d_p$) (mm) | Window diameter[a] ($d_w$) (mm) | Strut diameter[b] ($d_s$) (mm) | Specific surface area ($S_v$)[a] (m$^2$·m$^{-3}$) |
|---|---|---|---|---|---|
| 10 ppi | 0.67 | 5.35 ± 0.38 | 3.20 ± 0.77 | 2.21 | 544.48[a], 595.11[b] |
| 20 ppi | 0.77 | 3.45 ± 0.16 | 2.40 ± 0.58 | 1.10 | 785.71[a], 797.59[b] |
| 40 ppi | 0.79 | 2.37 ± 0.30 | 1.43 ± 0.39 | 0.73 | 1105.80[a], 866.00[b] |

250 ms.

Measurements were performed with a *TE* of 2.6 ms, $\delta$ of 0.25 ms, and $\Delta$ of 10 ms. Additionally, in some measurements a $\Delta$ *of* 20 ms was used. In order to increase the SNR, 32 averages were used for all the measurements with encoding gradients in axial and radial direction, where $z$ corresponds to the axial direction and $y$ corresponds to the radial direction of the foams. The total measurement time of each measurement was 8 min 23 s.

An in-house MATLAB (R2017b, The MathWorks, Inc., Natick, USA) script was used for processing the time-domain data. The propagator was calculated from the time-domain signal applying Hamming apodization and 1D Fourier transformation along the time domain, followed by peak integration and 1D Fourier transformation along variable $q$.

In order to estimate dispersion coefficients, several processing steps were performed. The baseline of the Fourier transformed spectra was corrected using a fifth-order function. Then, zero-order phase correction was applied for the one half (32 $q$-steps) of the spectra. Subsequently, the peak area was integrated and the obtained values were plotted against $b$-values to determine the dispersion coefficient at each flow rate. Alternatively, the dispersion coefficient was estimated from the FWHM value.

## 4. Result and discussion

The results are divided into two sections. Firstly, axial dispersion coefficients and secondly radial dispersion coefficients are investigated. In each section, the effect of flow rate, window size, strut diameter, open porosity, and VOI on gas displacement is evaluated.

### 4.1. Axial dispersion

#### 4.1.1. Flow rate effect

In Fig. 4, the gas propagators measured for 10, 20, and 40 ppi samples are normalized to constant area for better comparison. While the gas propagators form Gaussian distributions for lower flow rates, increasing asymmetry of the propagators is observed at higher flow rates. The calculated $\Delta L_{max}$ values show that in each sample the flow reaches the long displacement regime at higher flow rates [9]. Therefore, the dispersion coefficients, which have been obtained in the current analysis by measurements as described below, are suitable to be used in the convection diffusion equation (Eq. (1)) in numerical simulations.

As can be seen in Fig. 4, the propagators of all samples shift toward the flow direction and create peaks with positive displacement lengths. No stagnant peak and separation of flow due to dead pores occur as only one peak for each propagator is observed. The peaks of the propagators slightly move toward the flow direction as flow increases from 0.1 to 0.5 L·min$^{-1}$. In this range (0.1–0.5 L·min$^{-1}$) the $\Delta L_{max}$ of the gas ensemble is shorter or comparable to the window size of the foams, used as a characteristic length of the open-cell foams, indicating low interaction of gas flow with pore walls. In this stage the gas propagators indicate that only a small part of the gas molecules interacts with the sample [43]. The stepwise increase of the flow rate gradually affects the mixing length [12] and the displacement path of the gas in the foams. The peak of the propagators is continuously shifted toward the net flow direction. For higher flow rates, in particular for flow rates above 1.25 L·min$^{-1}$, the propagators show a wing or shoulder toward the flow direction and form asymmetrical displacement probabilities. For these flow rates, the $\Delta L_{max}$ is already longer than the window size of all the foams. The asymmetrical distribution of gas displacement corresponds to the transition between Gaussian distributions expected for low and sufficiently high flow rates [43].

In this study, no flow rate > 2.25 L·min$^{-1}$ was measured. However, it can be expected that at longer observation times the propagators again form a Gaussian distribution again indicating enough interactions

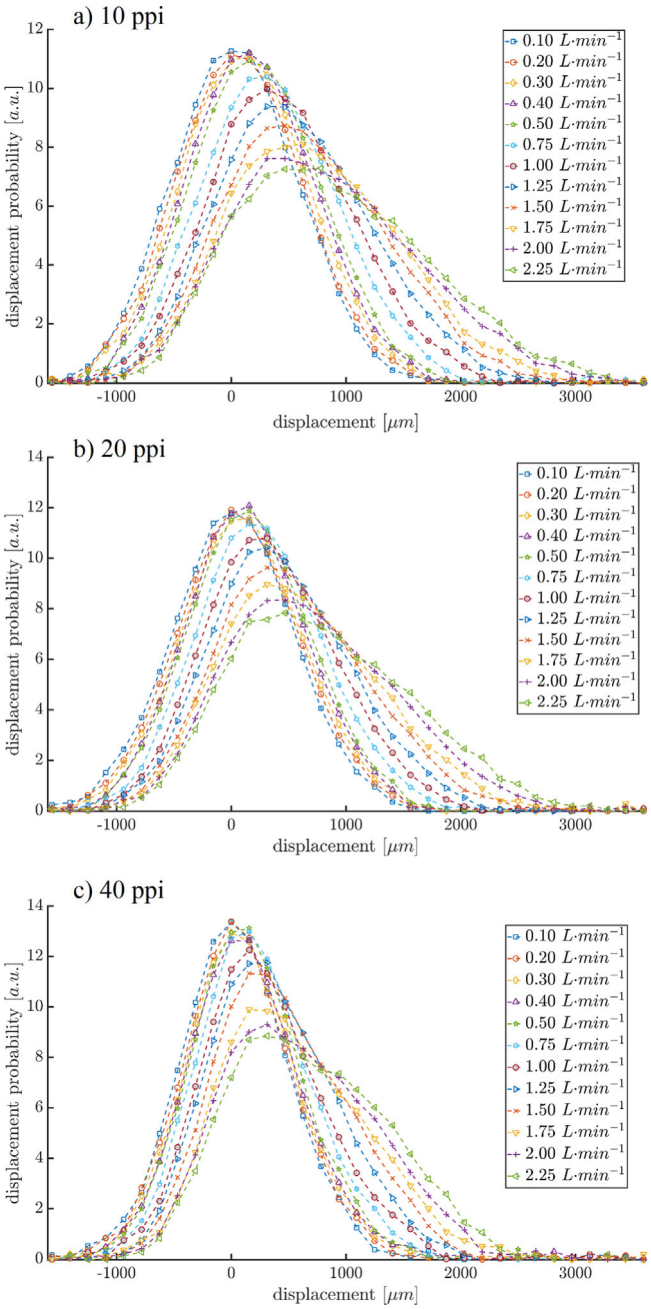


**Fig. 4.** Displacement probability at different flow rates for (a) 10 ppi, (b) 20 ppi, and (c) 40 ppi samples.

of gas with the interconnected network of the foams. Such a transition was observed by Koptyug et al. for the case of butane flow through glass beads [43]. Although the short $T_1$ relaxation time of methane severely affects the SNR, which thus limits the observation time, measurements performed at $\Delta$ = 20 ms show a tendency of forming Gaussian displacement functions (c.f. Appendix Fig. S1). For all measured flow rates, the $\Delta L_{max}$ of gas molecules increases with decreasing pore density ($\Delta L_{max(10\ ppi)} > \Delta L_{max(20\ ppi)} > \Delta L_{max(40\ ppi)}$), reflecting the different window size of samples obtained in μ-CT measurements ($d_{w(10ppi)=3.2mm} > d_{w(20ppi)=2.4mm} > d_{w(40ppi)=1.8mm}$).

For a quantitative comparison of all gas propagators FWHM values were used as an indicator of displacement width of the gas ensemble through the foams (c.f. Fig. 5). With increasing flow rate, FWHM increases non-linearly. The FWHM value allows to estimate the 'apparent dispersion coefficient' at the measured observation time using Eq. (5)

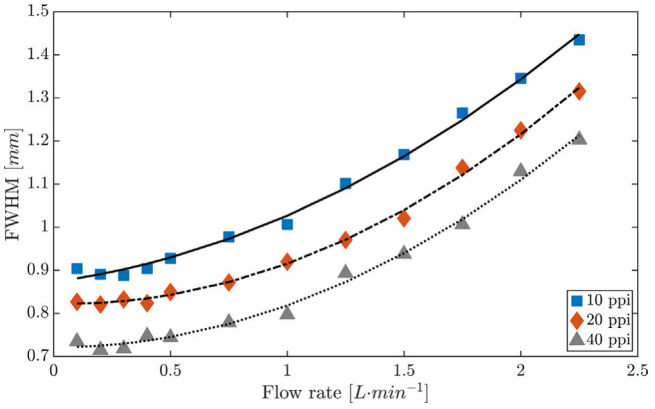


**Fig. 5.** Full width at half maximum (FWHM) of gas propagators at different flow rates in foams. The dashed lines show an exponential fit to the data obtained for each sample.

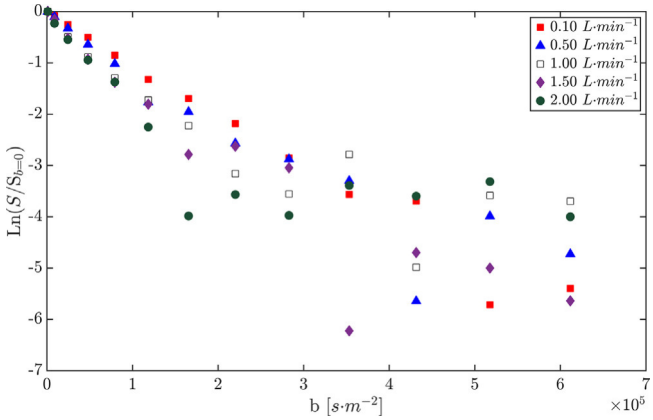


**Fig. 6.** Natural logarithm of the signal (peak area) as a function of *b*-value for the 20 ppi foam.

derived from a Gaussian distribution. Of course, using $D_{app}$, i.e., a single scalar parameter, simplifies the characterization of a complex, asymmetric displacement function. However, $D_{app}$ can be used in the numerical solution of the convection-diffusion equation (Eq. (1)). In the next subsection (4.1.2) we use $D_{app}$ to compare the dispersion process of gas for different foam samples, and a detailed description of the calculated axial dispersion coefficients is given in Section 4.1.3.

### 4.1.2. Diffusion and mechanically induced dispersion

Compared to turbulent flow, much smaller dispersion is expected for laminar flow. This is due to the non-mixing nature of the laminar gas flow. Dispersion consists of two components, diffusion and advection. The accuracy obtained in NMR measurements enables us to distinguish differences between dispersion mechanisms at different flow rates. The gradual increase in flow rate of foams (c.f., Fig. 4) helps to better distinguish the effects of diffusion and advection components on the displacement functions. Although the mean displacement path of gas generally increases when the flow rate increases, at very low flow rates ranging between 0.1 and 0.5 L·min$^{-1}$ (for all samples) no significant mechanically driven dispersion was observed. This finding can be better discussed when the apparent dispersion coefficients $D_{app}$ measured with flow are compared to effective diffusion coefficient $D_{eff}$ of methane measured without flow, which we measured in the same foams without flow obtaining $D_{eff}$ for 10, 20, and 40 ppi samples as follows [31]: $D_{eff\,(10ppi)} = (1.73 \pm 0.02) \times 10^{-5}$ m$^2$·s$^{-1}$, $D_{eff\,(20ppi)} = (1.53 \pm 0.05) \times 10^{-5}$ m$^2$·s$^{-1}$, and $D_{eff\,(40ppi)} = (1.48 \pm 0.03) \times 10^{-5}$ m$^2$·s$^{-1}$.

The obtained apparent dispersion coefficients for flow rates ranging from 0.1 to 0.5 L·min$^{-1}$ form a plateau (c.f., Fig. 5 and Table 2), while for flow rates > 0.75 L·min$^{-1}$ a remarkable increase in apparent dispersion coefficient of 20 and 10 ppi samples can be observed (c.f., Table.2). This trend occurs for 40 ppi foam at flow rates > 1.25 L·min$^{-1}$. Note that the minor differences between the measured $D_{app}$ for low flow rates and $D_{eff}$ determined in the previous study might be due to small variations between the samples from the same production line. For all samples, $D_{app}$ becomes larger than $D_{eff}$ for flow rates > 0.5 L·min$^{-1}$. This suggests that the diffusional component of flow is still the dominant mechanism of mass transport for the lower flow rates, while at higher flow rates (0.75 L·min$^{-1}$ in case of 10 and 20 ppi and 1.25 L·min$^{-1}$ for 40 ppi foam), mass transport is affected by the mechanically driven share of flow. The observed dependence of the FWHM values as a function of the flow corresponds to the transition from the Darcy regime ($Re_p < 1$) to the Darcy-Forchheimer flow regime, which occurs for flow rates ranging $1 < Re_p < 10$, i.e., up to flow rate of 0.5 L·min$^{-1}$. This observation underpins the reliability of the measurements to distinguish the transition between the two regimes based on the theory described in literature [39–41]. It is worth mentioning that for all flow rates a portion of negative displacement is observed. This can predominantly be caused by diffusion and in part, at least for higher flow rates, by back mixing.

### 4.1.3. Axial dispersion coefficient ($D_{\parallel}$)

The axial dispersion coefficients were determined by two methods. First, based on the obtained FWHM of the propagators (Eq. (5)) and second, from the slope of log-linear fit of the peak area versus *b*., i.e., signal attenuation (Eq. (2)) versus the applied *b*-value in each *q* step (Fig. 6). The linear part of the attenuation indicates Gaussian displacement, typically found as long as $b{\cdot}D \ll 1$ [23]. For the latter method, the frequency domain data was phase and baseline corrected to suppress flow effects on the methane spectra in all measurements (cf. Section 3.3).

Inspection of the signal attenuation in a 20 ppi sample in Fig. 5 shows steady increase in dispersion as a consequence of increased flow rate. The dispersion coefficients measured from FWHM of gas propagators were chosen based on two reasons. First, only the lowest four or five *q* values fulfill $b{\cdot}D < 1$ and could be used for the log-linear fit. Second, for higher flow rates a non-linear signal decay can be observed even in this low *b*-values range (c.f., Fig. 6). The determined axial dispersion coefficients can be compared with the effective diffusion coefficients reported in the previous publication [31]. As expected, the dispersion coefficients increase with increasing flow rate. The highest and the lowest $D_{\parallel}$ always belong to 10 and 40 ppi samples at identical flow rates, respectively.

### 4.1.4. Foam geometry and $D_{\parallel}$

The dispersion coefficient can be correlated to the geometry of each foam as a function of the flow rate or velocity (c.f., Fig. 4). Montillet

**Table 2**
Axial dispersion coefficient ($D_{\parallel} \times 10^5$ m$^2$·s$^{-1}$) obtained for three structures using FWHM values for flow rates ranging from 0.1 to 2.25 L·min$^{-1}$.

| L·min$^{-1}$ | 0.10 | 0.20 | 0.30 | 0.40 | 0.50 | 0.75 | 1.00 | 1.25 | 1.50 | 1.75 | 2.00 | 2.25 |
|---|---|---|---|---|---|---|---|---|---|---|---|---|
| 10 ppi | 1.71 | 1.66 | 1.65 | 1.71 | 1.79 | 2.00 | 2.12 | 2.54 | 2.86 | 3.35 | 3.79 | 4.31 |
| 20 ppi | 1.43 | 1.41 | 1.45 | 1.42 | 1.51 | 1.59 | 1.77 | 1.98 | 2.20 | 2.71 | 3.14 | 3.62 |
| 40 ppi | 1.12 | 1.07 | 1.08 | 1.17 | 1.16 | 1.28 | 1.32 | 1.67 | 1.84 | 2.13 | 2.67 | 3.02 |

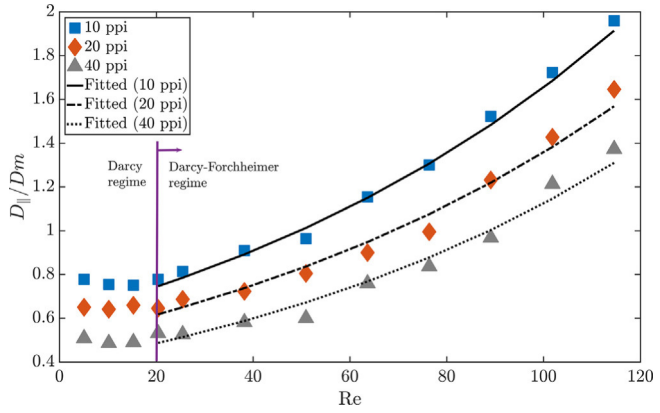


**Fig. 7.** Normalized axial dispersion coefficient as a function of *Re* number determined for the three foam types. The superimposed curves are exponential fits to the data.

et al. proposed a linear correlation between superficial velocity and axial dispersion of liquid flow in foams [44]. In some studies [25,45], the axial dispersion coefficient has been correlated to the flow-dependent Reynolds number using a power function, $D_{\parallel} = c \cdot \mathrm{Re}_p^n$, for fitting data measured for different pore sizes. $D_{\parallel}/D_m$ is illustrated for different flow rates as a function of *Re* being the usual scale for industrial approaches (Fig. 7). In addition, the ratio between $D_{\parallel}$ and self-diffusion of free methane gas $D_m = 2.24 \times 10^{-5}$ m$^2$·s$^{-1}$ is plotted [31] against *Pe* in the Appendix in Fig. S2. The Peclet number describes the ratio of mechanically driven flow to the rate of diffusion. An exponential function (Eq. (8)) is used to relate the *Re* or volumetric flow rate to the axial dispersion coefficient in the Darcy-Forchheimer regime as it gave a higher $R^2$ value compared to other tested functions.

$$D_{\parallel} = \alpha \cdot e^{\beta \cdot Re} \tag{8}$$

The values for $\alpha$ are detailed in Table 3 for 10, 20, and 40 ppi samples ($R^2 > 0.97$). For all fitted functions $\beta$ was equal to 0.01. The proposed correlation shows a high precision for fitting $D_{\parallel}$in the Darcy-Forchheimer regime, where the flow rate ranges between 0.5 and 2.25 L·min$^{-1}$, corresponding to $Re_p$ values between 2.40 and 24.80 for the samples analyzed.

The obtained results enabled a precise correlation between axial dispersion coefficient and *Re* within the measured flow in the Darcy-Forchheimer regime. The exponential fitting was chosen since it gave the best fitted curve (higher $R^2$ value) compared to linear or power functions mentioned in literature for dispersion of water in mesh wired metal foams [25]. Thus, the given correlation and the exponential fitting is merely achieved based on empirical data, without theoretical background. We do not claim that the exponential fit is suitable for extrapolation to higher flow rates of gas in foams.

#### 4.1.5. Window size and porosity effect

Beside intrinsic velocity, window size and open porosity are the most important parameters for characterizing mass transport in foams [46]. The first parameter primarily regulates the mixing length of dispersive flow in the structure, whereas the second mainly controls the flow hydrodynamics in the void space of the foam. However, since there is an interaction between window size and open porosity as reported in the literature [46], their effect cannot be fully decoupled and evaluated separately. Minor alteration in the morphology of foams may affect dispersion in both axial and radial directions. Accordingly, we analyzed the effect of window size and porosity on axial dispersion at different *Re*numbers. The window size effect on axial dispersion is compared in Fig. 8 for two *Re* numbers. For *Re* ~ 25 ($Re_p$ = 2.41–5.44), corresponding to flow rate of 0.5 L·min$^{-1}$, the dispersion is still dominated by diffusion (c.f., Fig. 8a). For *Re* ~ 76 ($Re_p$ = 7.24–16.34) using a flow rate of 1.5 L·min$^{-1}$, the dispersion is more affected by advection (c.f., Fig. 8b). Fig. 8 also contains the propagators measured on free methane gas with and without flow [31].

**Table 3**
Fitting constants for $D_{\parallel}$ versus *Re* using Eq. (7).

| Sample | $\alpha$ (mm$^2$·s$^{-1}$) |
|---|---|
| 10 ppi | 1.36 |
| 20 ppi | 1.11 |
| 40 ppi | 0.86 |

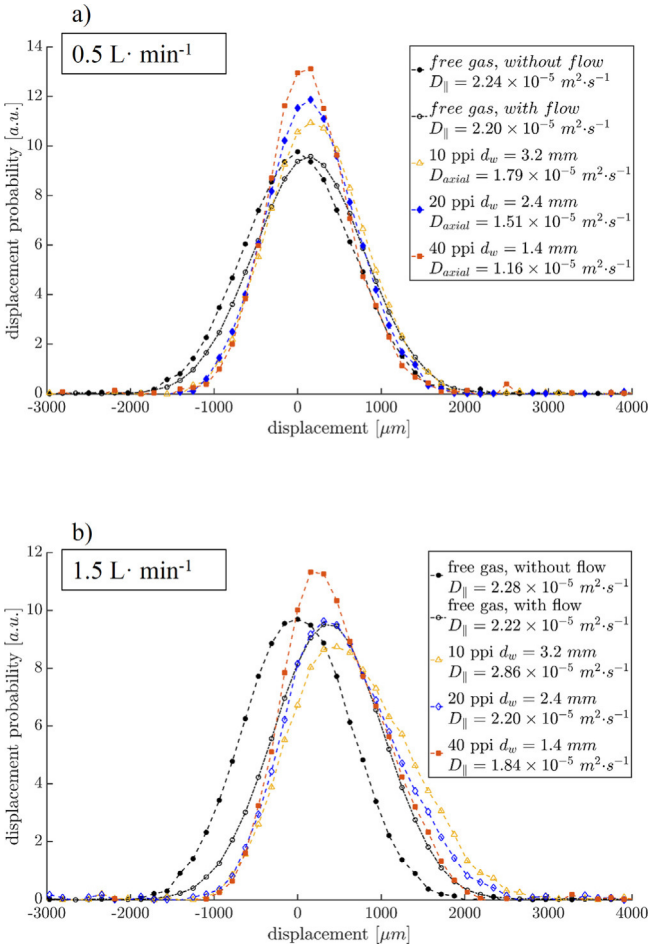


**Fig. 8.** Gas propagator of methane measured in samples with different pore density at (a) 0.5 and (b) 1.5 L·min$^{-1}$. For comparison, the values for free gas measured without and with flow are given. Note that the different values for free gas in *a* and *b* reflect the experimental error.

The results suggest that the extent of the hindrance of the gas molecules is connected to the windows size in foams considering that the peak of the displacement curves (c.f., Fig. 8b, flow rate of 1.5 L·min$^{-1}$) is observed at 156 μm, 312 and 877 μm for 10, 20 and 40 ppi samples, respectively. The gas propagator for the 40 ppi sample ($\varepsilon$ = 0. 79) forms the highest and narrowest peak. The pore connectivity also plays a significant role in dispersion of gas in the interconnected network of the foams as the tortuosity ($\tau = D_m/D_{eff}$) of the foam samples was measured ($\tau_{10ppi} < \tau_{20ppi} < \tau_{40ppi}$) for methane gas [31]. This shows that dispersion is affected by pore distribution and local heterogeneity of foams [47]. Furthermore, the comparison of the maximum displacement ($\Delta L_{\max(10\ ppi)} > \Delta L_{\max(20\ ppi)} > \Delta L_{\max\ (40\ ppi)}$) is in agreement with the properties of foams reported in Table 1. This trend remains consistent at different flow rates. On the other hand, the possibility of backflow and reflection of gas molecules in the reverse direction of flow

is connected to the pore density of samples at a certain flow rate. This can be elucidated by comparing the probability of negative displacement in Fig. 8b.

It is worth mentioning that in Fig. 8b, which shows data measured at higher *Re*, the gas flow in the 20 ppi foam forms the maximum at a similar position as for the flowing free gas. In addition, the obtained $D_{\parallel}$ is almost identical to the dispersion coefficient of flowing free gas. This behavior can be associated with the moderate window diameter of 20 ppi samples. A point-wise comparison of the displacement probabilities in propagators of free gas and gas flowing through the 20 ppi sample at 1.5 L·min$^{-1}$ shows an enhanced movement of gas toward the net direction of the gas flow. This finding is in remarkable agreement with a numerical μ-CT based simulation performed to obtain velocity fields in foams of the same production line as those used in the current study [48].

### 4.2. Radial dispersion

In this section, gas propagators in the radial direction of the foams are presented and radial dispersion coefficients are calculated. Finally, the effect of VOI size and position on the radial dispersion coefficient is discussed.

The gas propagators measured at an observation time of 10 ms are depicted in Fig. S3 in the Appendix. The stagnant peaks at zero and symmetric shapes of the curves confirm that there is no net flow in the radial direction. However, the propagators slightly broaden with increasing flow rate, but maintain their Gaussian shape ($R^2 > 0.98$). Yet the degree of the hindrance of gas in the samples can be related to the pore window and strut diameter of the foams reported in Table 1. The propagators of 10, 20, and 40 ppi samples reach the baseline at about 2.0, 1.8, and 1.3 mm, respectively.

The obtained values for radial dispersion coefficients are given in Table 4. Additionally, Fig. S4 of the appendix shows a plot of $D_{\perp}$ versus the applied flow rates. Although the radial dispersion is less sensitive to the alteration of velocity as compared to axial dispersion, it increases (flow rate $<$ 1.5 L·min$^{-1}$) when flow velocity increases (c.f., Table.4). The rise in dispersion coefficients can also be linked to the geometry of the foams in radial direction. In the majority of the measurements (0.1 L·min$^{-1}$ $<$ flow rate $<$ 1.5 L·min$^{-1}$), the radial dispersion measured for the samples with bigger window size is larger than for foams with smaller window size ($D_{\perp(10ppi)} > D_{\perp(20ppi)} > D_{\perp(40ppi)}$). Although no mathematical correlation between *Re* and $D_{\perp}$ can be drawn, a lower bound for radial dispersion can be seen (c.f., Fig. S4). A stepwise increase in flow rate increases the radial dispersion. However, the increase in $D_{\perp}$ is not pronounced as compared to $D_{\parallel}$.

## 5. Dependency on size and position of VOI

The conducted measurements determined the gas propagators at the central volume of the foams (VOI as shown in Fig. 2b). To show that the results are representative of the averaged behavior of gas in the foams, some experiments were performed with different size and position of the VOI. First, the position of the standard VOI (12 × 12 × 12 mm$^3$) was shifted by 20 mm in axial direction of the sample. Second, the size of the VOI was enlarged to 16 × 16 × 16 mm$^3$. For both cases, almost identical gas propagators were measured, indicating that the results with the standard VOI are representative of the foams and allow consistent dispersion analysis.

The evaluation of VOI size effects on the radial dispersion is crucial since it shows that the chosen VOI for the measurement is not affected by the reactor wall. Thus, an enlarged VOI (16 × 16 × 16 mm$^3$) was used to measure the gas propagators again and compare the results to those obtained on the standard VOI (12 × 12 × 12 mm$^3$). This comparison can be found in the Appendix (Fig. S5). Both propagators show a stagnant peak at zero in radial direction. Minor differences in the baseline of the propagators lead to minor increase of $D_{\perp}$. This increase in $D_{\perp}$ can be explained by small contributions of the bypass flow between wall and foams. The gas molecules near the wall may move with lower hindrance due to the open edges of the sample and the reactor wall. To illustrate the extent of wall effects on radial dispersion, a larger VOI, which covers the entire radius of foam in x- and y-axes was chosen. The displacement length of the gas ensemble increases more than for the VOI of 16 × 16 × 16 mm$^3$ showing a lower probability of zero displacement, indicating the effect of wall interactions and flow bypass in these measurements. These measurements confirm that the chosen standard VOI is suitable for radial dispersion measurements in foams, not including the wall interactions.

## 6. Conclusion

An optimized PFG-STE NMR sequence was applied in order to determine mass transport properties of thermally polarized gas flowing through commercial foam structures. The localized pore-scale analysis was used to determine dispersion coefficients in the both axial and radial directions for different flow rates. The analysis allowed investigating the effect of foam geometry, such as pore density, porosity, and window size on the gas dispersion and the underlying dispersion mechanism.

For the investigated foams and used flow rates, it can be concluded that, unlike radial dispersion coefficients, axial dispersion coefficients increase exponentially with flow rate. In addition, it was shown that, at higher flow rates $>$ 0.5 L·min$^{-1}$, the axial apparent dispersion coefficients are larger than the effective diffusion coefficients of methane in the foam structures. Both axial and radial apparent dispersion coefficients increase with window size.

It was shown that the NMR-based measurement technique is a reliable method for a quantitative determination of dispersion measurements. Furthermore, the concept presented here now allows a pore-scale analysis of gas flow within ceramic foams. As another advantage of volume selective NMR displacement measurements, artifacts caused by wall interactions and flow bypass can be avoided by adjusting the VOI.

## Declaration of Competing Interest

The authors declare that they have no known competing financial interests or personal relationships that could have appeared to influence the work reported in this paper.

## Acknowledgments

The project was supported by German Research Foundation (DFG) in the frame of Research Training Group GRK 1860 “Micro-, meso- and macro-porous nonmetallic Materials: Fundamentals and Applications”

**Table 4**
Radial dispersion coefficient ($D_{\perp} \times 10^5$, in m$^2$·s$^{-1}$) obtained for three structures.

| L·min$^{-1}$ | 0.10 | 0.20 | 0.30 | 0.40 | 0.50 | 0.75 | 1.00 | 1.25 | 1.50 | 1.75 | 2.00 | 2.25 |
|---|---|---|---|---|---|---|---|---|---|---|---|---|
| 10 ppi | 1.46 | 1.38 | 1.43 | 1.48 | 1.43 | 1.46 | 1.66 | 1.61 | 1.63 | 1.39 | 1.53 | 1.42 |
| 20 ppi | 1.35 | 1.36 | 1.39 | 1.45 | 1.36 | 1.34 | 1.38 | 1.39 | 1.40 | 1.43 | 1.43 | 1.49 |
| 40 ppi | 1.33 | 1.31 | 1.25 | 1.34 | 1.37 | 1.36 | 1.37 | 1.40 | 1.37 | 1.43 | 1.49 | 1.54 |

(MIMENIMA).

## Appendix A. Supplementary data

Supplementary data to this article can be found online at https://doi.org/10.1016/j.cej.2020.124234.

## References


[1] P.D. Eggenschwiler, D.N. Tsinoglou, J. Seyfert, C. Bach, U. Vogt, M. Gorbar, Ceramic foam substrates for automotive catalyst applications: Fluid mechanic analysis, Exp. Fluids 47 (2009) 209–222, https://doi.org/10.1007/s00348-009-0653-2.

[2] M.V. Twigg, J.T. Richardson, Theory and applications of ceramic foam catalysts, Trans. IChemE 80 (2002) 183–189, https://doi.org/10.1205/026387602753501906.

[3] Y. Peng, J.T. Richardson, Properties of ceramic foam catalyst supports: one-dimensional and two-dimensional heat transfer correlations, Appl. Catal. A Gen. 266 (2004) 235–244, https://doi.org/10.1016/j.apcata.2004.02.012.

[4] S. Zuercher, K. Pabst, G. Schaub, Ceramic foams as structured catalyst inserts in gas-particle filters for gas reactions-Effect of backmixing, Appl. Catal. A Gen. 357 (2009) 85–92, https://doi.org/10.1016/j.apcata.2009.01.020.

[5] M.V. Twigg, J.T. Richardson, Fundamentals and applications of structured ceramic foam catalysts, Ind. Eng. Chem. Res. 46 (2007) 4166–4177, https://doi.org/10.1021/ie061122o.

[6] F. Lucci, A. Della Torre, G. Montenegro, P.D. Eggenschwiler, On the catalytic performance of open cell structures versus honeycombs, Chem. Eng. J. 264 (2015) 514–521, https://doi.org/10.1016/j.cej.2014.11.080.

[7] R.M. Heck, S. Gulati, R.J. Farrauto, The application of monoliths for gas phase catalytic reactions, Chem. Eng. J. 82 (2001) 149–156, https://doi.org/10.1016/S1385-8947(00)00365-X.

[8] B. Kreitz, G.D. Wehinger, T. Turek, Dynamic simulation of the $CO_2$ methanation in a micro-structured fixed-bed reactor, Chem. Eng. Sci. 195 (2019) 541–552, https://doi.org/10.1016/j.ces.2018.09.053.

[9] L. Lebon, J. Leblond, J.P. Hulin, Experimental measurement of dispersion processes at short times using a pulsed field gradient NMR technique, Phys. Fluids. 9 (1997) 481–490, https://doi.org/10.1063/1.869208.

[10] J.M. Van Baten, J. Ellenberger, R. Krishna, Radial and axial dispersion of the liquid phase within a KATAPAK-S(R) structure: Experiments vs. CFD simulations, Chem. Eng. Sci. 56 (2001) 813–821, https://doi.org/10.1016/S0009-2509(00)00293-1.

[11] J.S. Chen, J.T. Chen, C.W. Liu, C.P. Liang, C.W. Lin, Analytical solutions to two-dimensional advection-dispersion equation in cylindrical coordinates in finite domain subject to first- and third-type inlet boundary conditions, J. Hydrol. 405 (2011) 522–531, https://doi.org/10.1016/j.jhydrol.2011.06.002.

[12] P.M. Singer, J. Mitchell, E.J. Fordham, Characterizing dispersivity and stagnation in porous media using NMR flow propagators, J. Magn. Reson. 270 (2016) 98–107, https://doi.org/10.1016/j.jmr.2016.07.004.

[13] L. Kiewidt, J. Thöming, Multiscale modeling of monolithic sponges as catalyst carrier for the methanation of carbon dioxide, Chem. Eng. Sci. X. 2 (2019), https://doi.org/10.1016/j.cesx.2019.100016.

[14] L. Kiewidt, J. Thöming, Pareto-optimal design and assessment of monolithic sponges as catalyst carriers for exothermic reactions, Chem. Eng. J. (2019) 496–504, https://doi.org/10.1016/j.cej.2018.11.109.

[15] P. Benz, P. Hütter, A. Schlegel, Radiale Stoffdispersionskoeffizienten in durchströmten keramischen Schäumen, Wärme- Und Stoffübertragung. 29 (1993) 125–127, https://doi.org/10.1007/BF01560081.

[16] C.L. Hackert, J.L. Ellzey, O.A. Ezekoye, M.J. Hall, Transverse dispersion at high Peclet numbers in short porous media, Exp. Fluids. 21 (1996) 286–290, https://doi.org/10.1007/BF00190679.

[17] J.C.F. Pereira, I. Malico, T.C. Hayashi, J. Raposo, Experimental and numerical characterization of the transverse dispersion at the exit of a short ceramic foam inside a pipe, Int. J. Heat Mass Transf. 48 (2005) 1–14, https://doi.org/10.1016/j.ijheatmasstransfer.2004.08.001.

[18] M. Saber, C. Pham-Huu, D. Edouard, Axial dispersion based on the residence time distribution curves in a millireactor filled with β-sic foam catalyst, Ind. Eng. Chem. Res. 51 (2012) 15011–15017, https://doi.org/10.1021/ie3017829.

[19] P. Habisreuther, N. Djordjevic, N. Zarzalis, Statistical distribution of residence time and tortuosity of flow through open-cell foams, Chem. Eng. Sci. 64 (2009) 4943–4954, https://doi.org/10.1016/j.ces.2009.07.033.

[20] C. Hutter, A. Zenklusen, S. Kuhn, P.R. von Rohr, Large eddy simulation of flow through a streamwise-periodic structure, Chem. Eng. Sci. 66 (2011) 519–529, https://doi.org/10.1016/j.ces.2010.11.015.

[21] R. Häfeli, C. Hutter, M. Damsohn, H.M. Prasser, P.R. von Rohr, Dispersion in fully developed flow through regular porous structures: Experiments with wire-mesh sensors, Chem. Eng. Process. Process Intensif. 69 (2013) 104–111, https://doi.org/10.1016/j.cep.2013.03.006.

[22] A.J. Onstad, C.J. Elkins, F. Medina, R.B. Wicker, J.K. Eaton, Full-field measurements of flow through a scaled metal foam replica, Exp. Fluids. 50 (2011) 1571–1585, https://doi.org/10.1007/s00348-010-1008-8.

[23] J.D. Seymour, P.T. Callaghan, Generalized approach to NMR analysis of flow and dispersion in porous media, AIChE J. 43 (1997) 2096–2111, https://doi.org/10.1002/aic.690430817.

[24] O. Levenspiel, Chemical reaction engineering, John Wiley & Sons, 1998.

[25] C. Hutter, A. Zenklusen, R. Lang, P.R. von Rohr, Axial dispersion in metal foams and streamwise-periodic porous media, Chem. Eng. Sci. 66 (2011) 1132–1141, https://doi.org/10.1016/j.ces.2010.12.016.

[26] M. Ferrari, C. Moyne, D. Stemmelen, Study of dispersion in porous media by pulsed field gradient NMR: Influence of the fluid rheology, Transp. Porous Media. 123 (2018) 101–124, https://doi.org/10.1007/s11242-018-1027-0.

[27] F. Stallmach, J. Kärger, The potentials of pulsed field gradient NMR for investigation of porous media, Adsorption 133 (1999) 117–133, https://doi.org/10.1023/A:1008949607093.

[28] A.T. Watson, C.T.P. Chang, Characterizing porous media with NMR methods, Prog. Nucl. Magn. Reson. Spectrosc. 31 (1997) 343–386, https://doi.org/10.1016/S0079-6565(97)00053-8.

[29] J.D. Seymour, P.T. Callaghan, "Flow-diffraction" structural characterization and measurement of hydrodynamic dispersion in porous media by PGSE NMR, J. Magn. Reson.-Ser. A. 122 (1996) 90–93, https://doi.org/10.1006/jmra.1996.0182.

[30] S.L. Codd, S.A. Altobelli, A PGSE study of propane gas flow through model porous bead packs, J. Magn. Reson. 163 (2003) 16–22, https://doi.org/10.1016/S1090-7807(03)00111-3.

[31] M. Mirdrikvand, J. Ilsemann, J. Thöming, W. Dreher, Spatially resolved characterization of the gas propagator in monolithic structured catalysts using NMR diffusiometry, Chem. Eng. Technol. 41 (2018) 1871–1880, https://doi.org/10.1002/ceat.201800201.

[32] R. Kimmich, F. Winter, W. Nusser, K.H. Spohn, Interactions and fluctuations deduced from proton field-cycling relaxation spectroscopy of polypeptides, DNA, muscles, and algae, J. Magn. Reson. 68 (1986) 263–282, https://doi.org/10.1016/0022-2364(86)90243-X.

[33] I. Tkáč, Z. Starčuk, I.Y. Choi, R. Gruetter, In vivo $^1$H NMR spectroscopy of rat brain at 1 ms echo time, Magn. Reson. Med. 41 (1999) 649–656, https://doi.org/10.1002/(SICI)1522-2594(199904)41:4<649::AID-MRM2>3.0.CO;2-G.

[34] D.G. Cory, A.N. Garroway, Measurement of translational displacement probabilities by NMR: An indicator of compartmentation, Magn. Reson. Med. 14 (1990) 435–444, https://doi.org/10.1002/mrm.1910140303.

[35] E.H.M.S.G. de Figueiredo, A.F.N.G. Borgonovi, T.M. Doring, Basic concepts of mr imaging, diffusion MR imaging, and diffusion tensor imaging, Magn. Reson. Imaging Clin. N. Am. (2011), https://doi.org/10.1016/j.mric.2010.10.005.

[36] P.T. Callaghan, D. MacGowan, K.J. Packer, F.O. Zelaya, High-resolution q-space imaging in porous structures, J. Magn. Reson. 90 (1990) 177–182, https://doi.org/10.1016/0022-2364(90)90376-K.

[37] J. Kärger, Transport phenomena in nanoporous materials, ChemPhysChem 16 (2015) 24–51, https://doi.org/10.1002/cphc.201402340.

[38] A. Inayat, H. Freund, T. Zeiser, W. Schwieger, Determining the specific surface area of ceramic foams: The tetrakaidecahedra model revisited, Chem. Eng. Sci. 66 (2011) 1179–1188, https://doi.org/10.1016/j.ces.2010.12.031.

[39] D.B. Ingham, I. Pop, Transport Phenomena in Porous Media III (1998), https://doi.org/10.1016/B978-0-08-044490-1.X5003-0.

[40] A. Della Torre, G. Montenegro, G.R. Tabor, M.L. Wears, CFD characterization of flow regimes inside open-cell foam substrates, Int. J. Heat Fluid Flow 50 (2014) 72–82, https://doi.org/10.1016/j.ijheatfluidflow.2014.05.005.

[41] D. Seguin, A. Montillet, J. Comiti, F. Huet, Experimental characterization of flow regimes in various porous media-II: Transition to turbulent regime, Chem. Eng. Sci. 53 (1998) 3897–3909, https://doi.org/10.1016/S0009-2509(98)80003-1.

[42] C.J. Jamson, A.K. Jameson, N.C. Smith, J.K. Hwang, T. Zia, Carbon-13 and proton spin relaxation in methane gas, J. Phyiscal Chem. 95 (1991) 1092–1098.

[43] I.V. Koptyug, A.A. Lysova, A.V. Matveev, V.N. Parmon, R.Z. Sagdeev, NMR imaging of mass transport processes and catalytic reactions, Top. Catal. 32 (2005) 83–91, https://doi.org/10.1007/s11244-005-9256-1.

[44] A. Montillet, J. Comiti, J. Legrand, Axial dispersion in liquid flow through packed reticulated metallic foams and fixed beds of different structures, Chem. Eng. J. 52 (1993) 63–71, https://doi.org/10.1016/0300-9467(93)80050-X.

[45] D.R.F. Harleman, R.R. Rumer, Longitudinal and lateral dispersion in an isotropic porous medium, J. Fluid Mech. 16 (1963) 385–394, https://doi.org/10.1017/S0022112063000847.

[46] L. Kiewidt, Solid sponges as support for heterogeneous catalysts in gas-phase reactions, (Doctoral dissertation), University of Bremen, 2017 https://d-nb.info/1150833947/34.

[47] C. D'agostino, J. Mitchell, L.F. Gladden, M.D. Mantle, Hydrogen bonding network disruption in mesoporous catalyst supports probed by PFG-NMR diffusometry and NMR relaxometry, J. Phys. Chem. C (2012), https://doi.org/10.1021/jp2123295.

[48] M. Niemeyer, Simulation der Strömungsverteilung in gleichfoermigen und gradierten Schwaemmen (Master Thesis), Univ. Bremen, 2016.